Nanoscale

PAPER

Check for updates

Biomass-derived substrate hydrogenation over rhodium nanoparticles supported on functionalized mesoporous silica†

Israel T. Pulido-Díaz, [a,b] Draco Martínez,[a] Karla P. Salas-Martin, [a] Benjamín Portales-Martínez, [d] Dominique Agustin, [b,c] Antonio Reina [a] and Itzel Guerrero-Ríos *[a]

The use of supported rhodium nanoparticles (RhNPs) is gaining attention due to the drive for better catalyst performance and sustainability. Silica-based supports are promising for RhNP immobilization because of their thermal and chemical stability. Functionalizing silica allows for the design of catalysts with improved activity for biomass transformations. In this study, we synthesized rhodium nanoparticles (RhNPs) supported on N-functionalized silica-based materials, utilizing SBA-15 as the support and functionalizing it with either nicotinamide or an imidazolium-based ionic liquid. Solid-state ^{29}Si and ^{13}C NMR experiments confirmed successful ligand anchoring onto the silica surface. RhNPs@SBA-15-Imz[NTf$_2$] and RhNPs@SBA-15-NIC were efficiently prepared and extensively characterized, revealing small, spherical, and well-dispersed fcc Rh nanoparticles on the support surface, confirmed by XPS analyses detecting metallic rhodium, Rh(I), and Rh(III) species. The catalytic performance of these materials is assessed in the hydrogenation of biomass-derived substrates, including furfural, levulinic acid, terpenes, vanillin, and eugenol, among others, underscoring their potential in sustainable chemical transformations. The nanocatalysts demonstrated excellent recyclability and resistance to metal leaching over multiple cycles. The study shows that neutral and ionic silica grafting fragments differently stabilize RhNPs, affecting their morphology, size, and interaction with silanol groups, which impacts their catalytic activity.

aDepartamento de Química Inorgánica y Nuclear, Facultad de Química, UNAM, Circuito Escolar S/N, Coyoacán, Cd. Universitaria, 04510 Ciudad de México, Mexico. E-mail: itzelgr@unam.mx

bCentre National de la Recherche Scientifique (CNRS), Laboratoire de Chimie de Coordination (LCC), Université de Toulouse, UPS, INPT, 205, route de Narbonne, 31077 Toulouse, France

cUniversité de Toulouse, IUT P. Sabatier, Département de Chimie, Av. G. Pompidou, BP 20258, 81104 Castres CEDEX, France

dCONACYT, Centro de Investigación en Ciencia Aplicada y Tecnología Avanzada, Laboratorio Nacional de Conversión y Almacenamiento de Energía, Instituto Politécnico Nacional, Calzada Legaría 694, Col. Irrigación, Ciudad de México, 11500 Mexico

†Electronic supplementary information (ESI) available: Characterization spectra of silicas (TGA, IR, BET, and NMR) and RhNPs (IR, TGA, BET, SEM, TEM, XPS, and EDX), tables of selected catalytic reactions, and NMR results of products. See DOI: https://doi.org/10.1039/d4nr02579b

Introduction

The depletion of non-renewable fossil resources and the increase in environmental pollution have compelled the scientific community to focus on sustainable concepts, especially for the production and use of renewable chemicals.[1] Biomass, as the organic carbon source on Earth, holds significant importance in this regard.[2,3] Lignocellulosic biomass is the primary component of non-edible biomass, composed mainly of lignin, cellulose, hemicellulose, and lignocellulose. Lignin is the biopolymer that constitutes the main source of aromatics in nature.[4–7] Consequently, the conversion of lignin into chemicals, fuels, and carbon-based functional materials has become a topic of great importance.[8,9] In this context, lignin upon depolymerization produces phenolic monomers, which can be hydrogenated to access added-value oxygenated molecules, representing an interesting strategy to valorize biomass.[6,10–14] As an example, the valorization of lignin-derived phenol through hydrogenation produced cyclohexanone and cyclohexanol,[25,26] which are intermediates in the synthesis of caprolactam and adipic acid, both key materials for the industrial production of nylon.[30] One of the main issues in these processes is the lack of selectivity due to the formation of several side-products. Starting from complex carbohydrates like starch, cellulose, and hemicellulose, we can easily obtain oxygen-rich materials and convert them into renewable building blocks.[15] Reduction of substrates like furan-based substrates,[10] levulinic acid,[16–22] 5-hydroxymethyl-furfural,[23] sorbitol,[24] and others[27–29] facilitates the production

of biofuels and important intermediates in the synthesis of fine chemicals.

Rhodium-based catalysts favor a wide range of chemical transformations, including hydrogenations, hydroformylations, and carbonylations,[31–34] finding applications in various industrial processes. From a sustainable context, catalysts are not only required to perform under mild conditions but also enhance their performance, especially through their prolonged shelf-life through reuse and recycling. Supported rhodium nanoparticles (RhNPs) fulfill these requirements.[6] RhNPs have been successfully supported in various ways, including liquid phases, such as ionic liquids[35] and glycerol,[36,37] or solid phases, including activated carbon,[41,42] alumina,[43] polystyrene[44] and silica.[38–40] Silica-based supports offer thermal and chemical stability for catalysts and present a wide morphology diversity. In addition, functionalization of silica with coordinating molecules enables the immobilization of molecular catalysts and metal nanoparticles through interactions between catalytically active objects and modified supports.[45–51]

Indeed, functionalization permits the rational design and tuning of silica-based materials, yielding novel materials with higher activity for biomass transformations.[52] In our group, we have recently shown that RhNPs supported on N-functionalized MCM-41 silica facilitate the hydrogenation of several functional groups, including challenging substrates such as quinolines, nitriles, phenols, aldehydes, and ketones, under mild conditions.[53] In addition, bare MCM-41 does not stabilize RhNPs, and agglomerates of rhodium nanoparticles do not exhibit activity or selectivity comparable to the catalysts supported on N-functionalized MCM-41. Herein, rhodium nanoparticles supported on SBA-15 functionalized with nicotinamide and an imidazolium-based ionic liquid are studied, from synthesis and characterization to their catalytic evaluation in the hydrogenation of biomass-derived substrates including furfural, levulinic acid, terpenes, vanillin, and eugenol, among others.

Results and discussion

Catalyst synthesis and characterization

Organo(triethoxy)silane derivatives bearing nicotinamide (NIC) or imidazolium salt (Imz[NTf$_2$]) as the terminal function were grafted on silica through silanization (Scheme 1) using classical methods.[54,55]

FT-IR (ATR) analysis of silica-based materials (Fig. S1†) showed typical signals of the silica backbone (siloxane, silanol groups, and physisorbed water). For SBA 15-Imz[NTf$_2$], distinct signals corresponding to the imidazole ring (1574 cm^{-1}) and bistriflimide anion (1345 cm^{-1}, 1184 cm^{-1}, and 952 cm^{-1}) were identified.[56] For SBA 15-NIC, a prominent band was observed at around 1646 cm^{-1}, indicative of the stretching vibration of the amide carbonyl group, along with a minor signal at 1545 cm^{-1} corresponding to the N–H bending vibration.[53] The amount of ligand grafted on SBA-15 was determined through thermogravimetric analysis and elemental ana-
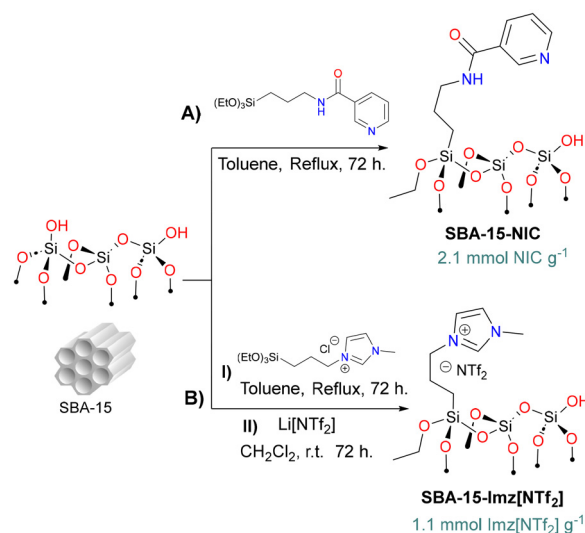
Scheme 1 Synthesis of functionalized silica-based supports: (A) SBA-15-NIC and (B) SBA-15-Imz[NTf$_2$].

lysis obtaining *ca.* 33 and 25 wt% for SBA 15-Imz[NTf$_2$] and SBA 15-NIC, respectively (Fig. S5†).

Solid-state ^{29}Si and ^{13}C NMR spectroscopy provided extra information about the degree of functionalization with either nicotinamide (NIC) or imidazolium salt (Imz[NTf$_2$]). The ^{29}Si UDEFT (Uniform Driven Equilibrium Fourier Transform) technique[57] was selected to perform quantitative one-dimensional ^{29}Si NMR experiments under magic-angle spinning (MAS) conditions. The NMR spectra of functionalized silica materials (Fig. 1) display three distinct resonances at −94 ppm (Q^2), −102 ppm (Q^3) and −111 ppm (Q^4), which correspond to the silica backbone. Additionally, another two resonances at −57 ppm (T^2) and −67 ppm (T^3) are attributed to the grafted organosiloxanes.[58] The prevalence of T^n peaks over Q^n confirms that the ligands are effectively condensed as a part of the silica framework.[59] The deconvolution of quantitative ^{29}Si NMR spectra allows for the estimation of silane grafting percentages, which are found to be 11.4% for SBA-15-Imz[NTf$_2$] and 12.9% for SBA-15-NIC. Furthermore, the integration of multiple techniques, including elemental analysis, thermogravimetric analysis, and adsorption/desorption isotherms, in conjunction with ^{29}Si NMR, enables the calculation of surface coverage by ligands (see ESI Table S1†). This analysis reveals approximately 2.4 and 3.9 molecules per nm^2 for SBA-15-Imz[NTf$_2$] and SBA-15-NIC, respectively. These findings indicate that the grafting process is significantly influenced by the type of organic moiety on the silane, with the NIC moiety leading to greater surface coverage on the silica material.

^{13}C CP-MAS NMR spectra confirmed the presence of the corresponding ligand for each material (Fig. S8†). Characteristic signals corresponding to the imidazole ring (134.6 ppm, 120.9 ppm, and 34.9 ppm) and the nicotinamide moiety (165 ppm and 123–147 ppm) were observed for SBA-15-Imz[NTf$_2$] and SBA-15-NIC, respectively.

Fig. 1 ^{29}Si UDEFT-MAS NMR spectra of SBA-15-Imz[NTf$_2$] (A) and SBA-15-NIC (B). Inset: schematic representing surface grafting possibilities for organosiloxanes on silica.

The as-prepared materials were employed for rhodium nanoparticle immobilization. RhNPs were obtained through the decomposition of the organometallic precursor methoxy (cyclooctadiene) rhodium(I) dimer [Rh(μ-OMe)(1,5-COD)]$_2$ under hydrogen pressure (Scheme 2). Nanoparticles were synthesized under mild conditions (3 bar H$_2$ at room temperature) in the presence of functionalized SBA 15-N, yielding air-stable black powders containing 10 wt% of Rh. Far-IR spectroscopy showed a characteristic signal at 462 cm^{-1} corresponding to the rhodium–nitrogen stretching vibration, pointing out the coordination of metal nanoparticles to the grafted ligand (Fig. S4†).[60]

Scheme 2 General synthesis of RhNPs@SBA-15-N.

High-angle annular dark-field scanning transmission electron microscopy (HAADF-STEM) of the supported RhNPs showed pseudo-spherical, small, and well-dispersed particles for both materials (Fig. 2). RhNPs@SBA-15-Imz[NTf$_2$] and RhNPs@SBA-15-NIC showed very small nanoparticles with a mean diameter of 2.7 ± 0.6 nm and 1.7 ± 0.3 nm, respectively. In both cases, nanoparticles were located at the surface and in the pores of the functionalized silica-based support, and narrow-size distributions were obtained. STEM images together with electronic diffraction analysis and fast-Fourier transform evidenced the face-centered cubic (fcc) crystalline structure of metallic Rh(0), where the measured interplanar distance (0.22 nm) corresponded to the crystallographic {111} planes (Fig. S9 and S11†). EDX elemental mapping showed the presence of Rh and N homogeneously dispersed within the silica surface (Fig. 2). These results confirm the correct grafting of the ligands and the homogeneous dispersion of RhNPs. Complementary powder XRD analysis of RhNPs@SBA-15-Imz[NTf$_2$] (see ESI Fig. S7†) revealed an average crystal size of *ca.* 2.9 nm for Rh, as calculated using the Scherrer equation, which is consistent with values measured by HR-TEM. Although the silica mesoporous structure was retained throughout functionalization, showing a type IV isotherm with an H1 hysteresis loop in the N$_2$-adsorption–desorption isotherms (Fig. 3 and S6†),[53,61] a further decrease in the surface area of RhNPs@SBA-15-Imz[NTf$_2$] was observed. Interestingly, although the material exhibited a type IV isotherm, the hysteresis loop was classified as type H2,[62] revealing more complex pore structures associated with blockage in a narrow range of pore necks and the pore mouth (aperture) of the original functionalized silica by the Rh nanoparticles.[53,61] Pore size distributions of the samples (inset, Fig. 3) were estimated using the Barrett–Joyner–Halenda (BJH) method, revealing a pore distribution in the range of 2–5 nm.

The X-ray photoelectron spectroscopy (XPS) survey spectrum confirmed the presence of nitrogen and rhodium (Fig. S17 and S19†). The high-resolution spectrum of RhNPs@SBA-15-Imz[NTf$_2$] in the binding energy region corresponding to nitrogen (N 1s, Fig. S18†) exhibited three signals corresponding to the imidazole nitrogen (401.3 eV), bistriflimide nitrogen (399 eV) and a nitrogen with lower binding energy possibly due to coordination to rhodium (397.8 eV). The binding energy region of rhodium (Rh 3d$_{3/2}$ and Rh 3d$_{5/2}$) showed a mixture of Rh(0) (307.4 eV), Rh(I) (308.5 eV) and Rh(III) (310.0 eV) (Fig. 4). As shown, there is a high amount of Rh(0) in both materials. However, the Imz[NTf$_2$] ligand exhibited a higher ability to prevent rhodium from oxidation, which is in agreement with the superior catalytic activity in hydrogenation reactions (*vide infra*).

Catalytic activity in hydrogenation reactions

To evaluate the potential for biomass substrate valorization, the starting reaction investigated was phenol (**1**) hydrogenation, chosen as a model substrate for molecules obtained from lignin.
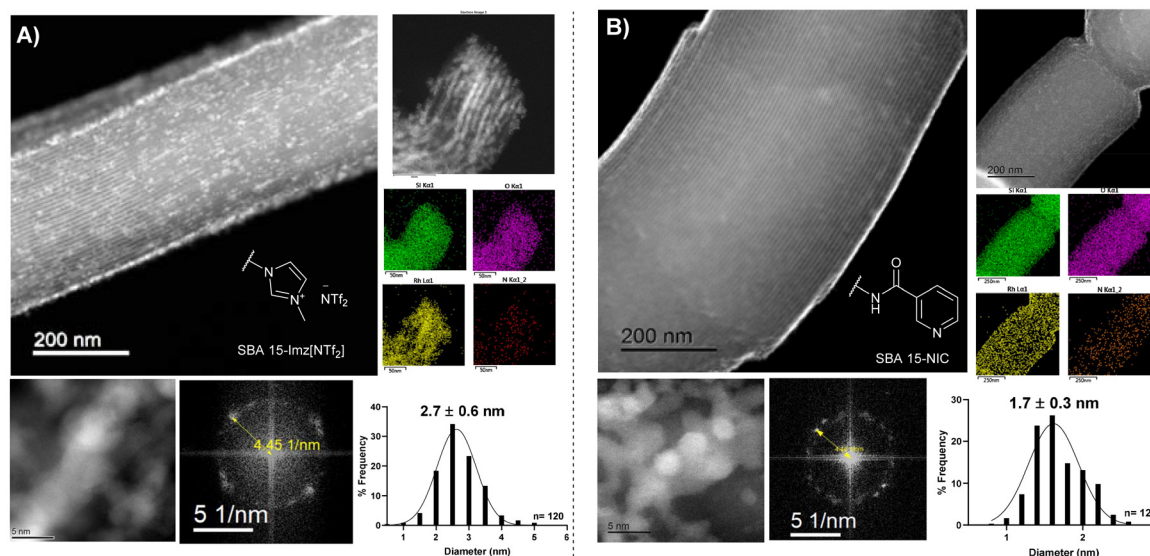
Fig. 2 HAADF-STEM micrographs, along with the corresponding FFT analysis, EDX elemental mapping, and size distribution histograms of RhNPs@SBA-15-Imz[NTf$_2$] (A) and RhNPs@SBA-15-NIC (B).
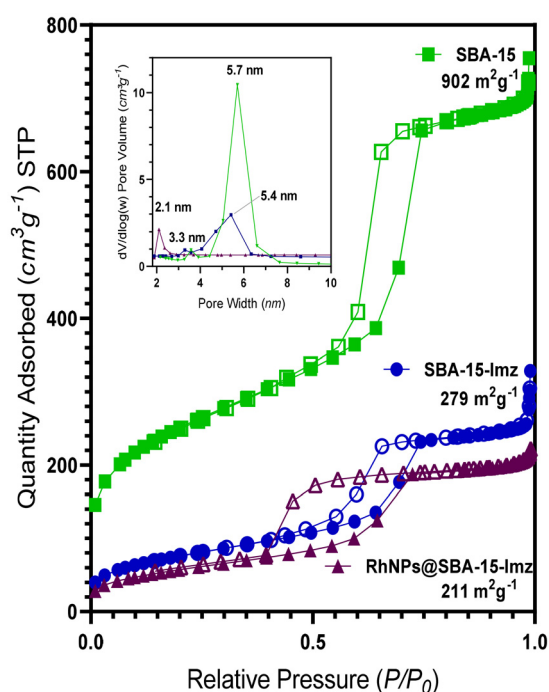

Fig. 3 Adsorption–desorption N$_2$ isotherms at 77 K of SBA-15 (green squares), SBA-15-Imz[NTf$_2$] (blue circles) and RhNPs@SBA-15-Imz[NTf$_2$] (purple triangles) and pore size distribution curves (inset, the pore width was estimated using the BJH model, cylindrical pores). Filled figures correspond to adsorption and hollow figures correspond to desorption.

Fig. 4 High-resolution XPS analysis in the binding region corresponding to rhodium. Rh 3d for RhNPs@SBA-15-Imz[NTf$_2$] (A) and RhNPs@SBA-15-NIC (B).

Phenol (**1**) was successfully hydrogenated under mild conditions (5 bar H$_2$, 100 °C for 4 h) with moderate selectivity to cyclohexanone (**1a**) (Table 1). It must be noticed that such reduction was not possible using RhNPs supported on functionalized MCM-41, showing the importance of the silica-based support nature.[53] To further investigate the importance of mesostructured pores in silica, RhNPs supported on disordered microporous silica such as silica gel or non-porous silica like Stöber demonstrated low activity in the hydrogenation of phenol. Similarly, RhNPs supported on pristine SBA-15, which lacks nicotinamide functional groups and consequently suffers from poor RhNP stability, as previously

Table 1 RhNP catalyzed hydrogenation of phenol

Entry	Catalyst	Conv.[a] (%)	Yield **1a**[a] (%)	Yield **1b**[a] (%)	TON[b]
1	RhNPs@SBA-15-Imz[NTf$_2$]	>99	67	33	265
2	RhNPs@SBA-15-NIC	>99	73	27	289
3[c]	RhNPs@MCM-41-NIC	25	66	32	92
4	RhNPS@SiO$_2$-gel-NIC	3	70	29	8
5[d]	RhNPs@Stöber-NIC	<1	54	10	n.d
6[e]	RhNPs@SBA-15	10	77	15	31
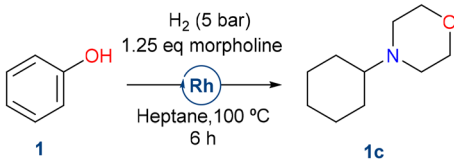
Reaction conditions: 2 mmol phenol, 5 mg catalyst (0.25 mol% for RhNPs@SBA-15-Imz[NTf$_2$] and RhNPs@SBA-15-NIC; 0.18 mol% for RhNPs@ MCM-41-NIC), 2 mL of heptane, H$_2$ (5 bar), 100 °C, and 4 h. [a] Determined by GC-FID. [b] TON = mmol of cyclohexanone per mmol of Rh. [c] From ref. 53. [d] 35% of benzene was detected. [e] 8% of benzene was detected.

Table 2 RhNP catalyzed tandem reductive amination of phenol

Entry	Catalyst	Conv.[a] (%)	Yield **1c**[a] (%)	TON[b]
1	RhNPs@SBA-15-Imz[NTf$_2$]	>99	98	392
2	RhNPs@SBA-15-NIC	>99	97	384
3[c]	RhNPs@MCM-41-NIC	84	78	364

Reaction conditions: 2 mmol phenol, 2.5 mmol morpholine, 5 mg catalyst (0.25 mol% for RhNPs@SBA-15-Imz[NTf$_2$] and RhNPs@SBA-15-NIC; 0.18 mol% for RhNPs@ MCM-41-NIC), 2 mL of heptane, H$_2$ (5 bar), 100 °C, and 6 h. [a] Determined by GC-FID. [b] TON = mmol of products per mmol of Rh. [c] From ref. 53.

reported,[53] showed no conversion or selectivity. In contrast to other reported catalysts, the ones presented herein favored the formation of the semi-hydrogenated ketone (**1a**) instead of the fully reduced cyclohexanol (**1b**).[63]

Taking advantage of the slow reduction to cyclohexanol (**1b**), we could prepare a tertiary amine in high yields by reductive amination. Utilizing reductive amination, substituted amines are synthesized from aldehydes or ketones along with less substituted amines.

This eco-friendly methodology prevents the need for reactive and potentially genotoxic reagents such as alkyl halides and sulphonates, commonly employed in conventional SN$_2$-type reactions of amines with alkylating agents. Furthermore, it mitigates concerns related to over-alkylation.[64] In this case, the condensation between the formed ketone (**1a**) and morpholine, followed by the hydrogenation of the enamine, is presented (Scheme 3).[65–68]

Both catalysts yielded the corresponding 4-cyclohexylmorpholine (**1c**) with complete phenol conversion, high selectivity towards **1c**, and a high turnover number (TON)

(Table 2). As mentioned above, those materials had superior activity compared to RhNPs supported on functionalized MCM-41.[53] Being slightly more active, RhNPS@SBA-15-Imz [NTf$_2$] was selected for recycling experiments and scope broadening of the reaction.

To evaluate the robustness and reusability of RhNPS@SBA-15-Imz[NTf$_2$] (Fig. 5), we conducted the reductive amination of phenol (**1**) with morpholine and also the reduction of cyclohexene as benchmark reactions (ESI, Scheme 1†). In the case of reductive amination of phenol and morpholine, no significant loss of activity or selectivity was observed during the first 3 runs, with excellent yields of the desired product (Fig. 5A).

Activity decreased on the 4th run, likely due to the accumulation of morpholine on the catalyst surface, poisoning its activity. Nevertheless, a cumulative TON of 2633 could be achieved. In contrast, cyclohexene (**2**) hydrogenation (ESI, Scheme 1†) remained constant after 5 runs, showing that the catalyst was still active and certainly not poisoned, reaching a cumulative TON of 3976.

HAADF-STEM micrographs of the catalyst after the catalytic reductive amination of phenol and morpholine did not exhibit any sign of RhNP agglomeration or metal leaching (Fig. S16†). Moreover, TEM images of the spent catalyst still show {111} crystallographic planes for fcc Rh(0), verified by the FFT of RhNPs (ESI Fig. S16†). In addition, rhodium was not detected by MP-AES analyses of the organic phase after the hydrogenation reaction, proving no metal leaching. These results highlight the important role of silica-supported N-stabilizers in the design for easy recycling applications and extending catalyst shelf-life.

Comparing the results obtained in this work with those found in the literature (Table 3), we observed a superior activity of Rh nanoparticles in terms of TON (Table 3, entries 9–12). This can be attributed to their high rhodium π-acidity,[76,77] allowing strong interactions of aromatic rings, which facilitate efficient hydrogenation processes. The integration of RhNPs
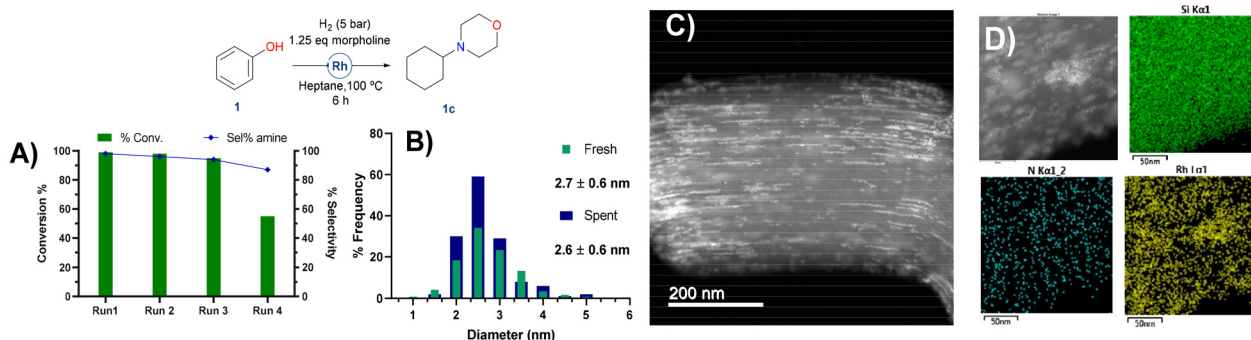

Scheme 3 RhNP catalyzed reductive amination of phenol and morpholine.

Fig. 5 (A) Recycling of the RhNPs@SBA-15-Imz[NTf$_2$] catalyst for the reductive amination of phenol; (B) RhNP size distribution (E; n = 120 particles) of the spent catalyst; (C) HAADF-STEM image (200 nm) and (D) EDX elemental mapping of spent RhNPs@SBA-15-Imz[NTf$_2$].

Table 3 Collection of data from the literature on phenolic derivative reductive amination catalyzed by metal nanoparticles

Entry	MNPs	Support	p of H$_2$ (bar)	Amine eq.	Temp. (°C)	Time (h)	Metal amount (mol%)	Solvent	Conv. (%)	Yield (%)	TON^a	TOF^b (h^{-1})	Ref.
1	Pd	C	None^c	2.0	60	6	9.00	H$_2$O	100	96	11	1.8	66
2			None^d	1.2	120	24	7.00	Toluene	—	90	13	0.5	69
3			20	2.5	140	24	6.00	m-Xylene	99	99	17	0.7	68
4			10	1.5	90	6	3.00	m-Xylene	>99	>99	33	5.5	67
5			5	1.1	100	15	2.00	H$_2$O	—	85	43	2.9	70
6			1	1.0	60	6	2.00	p-Xylene	—	84	43	7.2	71
7		Al$_2$O$_3$	1	2.0	70	10	9.30	Hexane	95	94	11	1.1	72
8	Ni		8	1.4	160	3	10.00	Toluene	99	99	10	3.3	73
9	Rh	C	1.5	1.4	120	20	2.10	t-Amyl alcohol	>99	64	65	3.3	74
10		PVP	5	1.4	40	24	2.00	H$_2$O	>99	96	48	2	75
11		SBA-15-Imz[NTf$_2$]	5	1.25	100	6	**0.25**	Heptane	>99	98	**392**	65	This work
12		SBA-15-NIC	5	1.25	100	6	**0.25**	Heptane	>99	97	**384**	64	

^{a} Data found in the corresponding reference; TON = mmol of amine per mmol metal. ^{b} TOF = TON per h. ^{c} HCOONa (20 equiv.) was used as a reductant. ^{d} HCOONa (6 equiv.).

into molecularly modified silica matrices further enhances their catalytic performance by providing a robust and high-surface-area support that stabilizes the nanoparticles and optimizes their dispersion. This setup ensures that the catalytic sites remain highly accessible, leading to improved turnover numbers (almost 6 times higher) and turnover frequencies (TOF, 20 times higher), as evidenced by the experimental data (Table 3, entries 11 and 12), showing substantial increases in conversion and yield percentages. Moreover, the tailored surface chemistry of imidazolium and nicotinamide moieties allows for precise interaction with complex biomass-derived molecules, thereby enhancing selectivity and reducing undesired side reactions.

With this catalyst in hand, we broadened the reaction scope of alkene derivatives (see Fig. 6) as well as other functional groups (Fig. 7 and 8). Styrene (**3**) and a range of biomass-derived alkenes, such as limonene (**4**), α-pinene (**5**), safrole (**6**), estragole (**7**), and eugenol (**8**), underwent facile hydrogenation

under mild conditions and low metal loadings (see Fig. 6, conditions A: heptane, 5 bar H$_2$, 3 h). However, terpene derivatives like geraniol (**9**), a primary component of rose essential oil, and myrcene (**10**), found in parsley essential oil, needed harsher conditions to achieve complete hydrogenation (conditions B: heptane, 20 bar H$_2$, 8 h). Remarkably, under solventless conditions, the double bonds of oleic acid (**11**) and squalene (**12**) were efficiently hydrogenated to yield very high conversion rates, demonstrating the robustness of RhNPs@SBA-15-Imz[NTf$_2$].

Other functional groups could also be hydrogenated with this catalytic system, including nitriles, nitro compounds, aromatics, and quinoline (Fig. 7). Benzonitrile (**13**) was reduced to benzylamine under standard conditions (20 bar H$_2$, 2 h) in the presence of 2 equivalents of ammonium hydroxide. As previously reported, the addition of aqueous ammonia prevents the formation of dibenzylamine and drives the reaction to benzylamine selectively.[78,79] Nitrobenzene (**14**) was hydrogenated
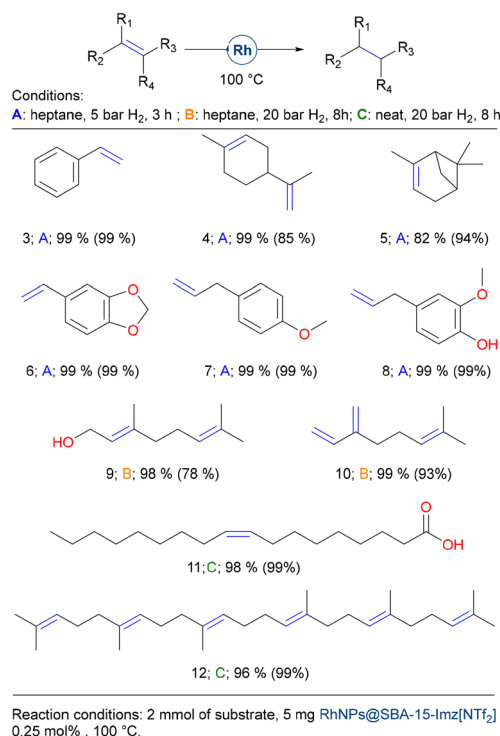
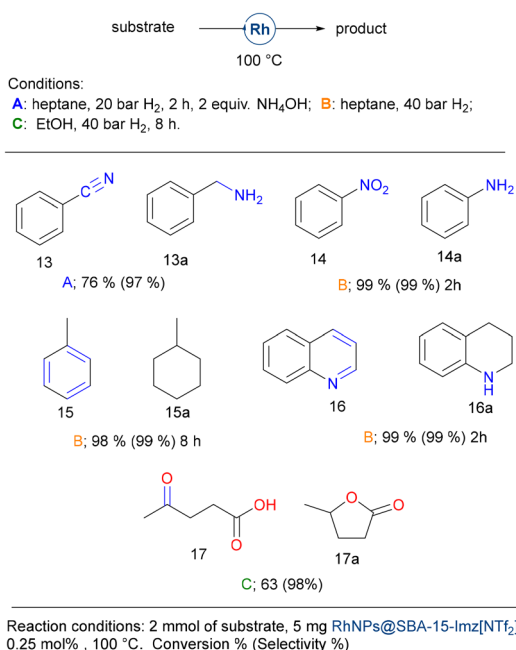Fig. 6 RhNP catalysed hydrogenation of biomass-derived alkenes.

Fig. 7 RhNP catalyzed hydrogenation of different functional groups.

Fig. 8 RhNP catalyzed hydrogenation of biomass-derived aldehydes.

to yield aniline (**14a**) under high hydrogen pressure (40 bar H$_2$), while no traces of cyclohexylamine were detected during nitrobenzene hydrogenation. Interestingly, aromatics bearing electron-donor groups could also be reduced under these harsher conditions. Indeed, toluene (**15**) gave methyl-
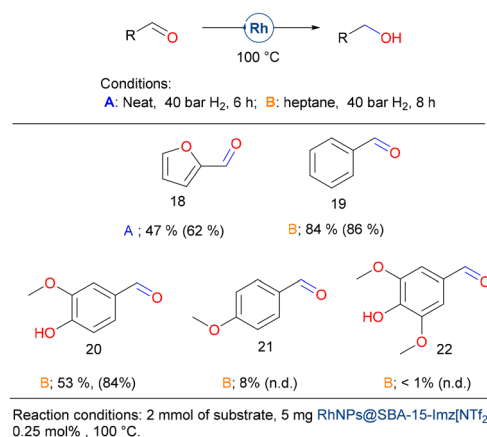
cyclohexane (**15a**) in high yields and quinoline (**16**) gave 1,2,3,4-tetrahydroquinoline (**16a**). Levulinic acid (**17**), being a molecule potentially obtained from the starch of ligno-cellulose, was hydrogenated in a moderate yield but with excellent selectivity to γ-valerolactone (**17a**), used as a solvent or in the perfume industry.[80]

Finally, we evaluate the hydrogenation of biomass-derived aldehydes (Fig. 8). Furfural (**18**) is one of the most promising biomass-derived platform molecules with great potential to produce fuel additives and high-value chemicals. Among its various transformations, the catalytic hydrogenation of furfural into furfuryl alcohol stands out as a crucial process in the chemical conversion of bio-derived compounds.[81] In pursuit of environmentally sustainable alternatives, supported noble and transition-metal catalysts, including Pt,[82] Ir,[83] Pd,[84] Ru,[85] Ni,[86] Co,[87] and Rh,[88] and other bimetallic systems have been explored. These catalysts offer the potential to selectively hydrogenate the carbonyl group while preserving the carbon–carbon double bonds. However, many of these catalysts require elevated temperatures and/or the use of acid additives, which can be limiting factors for their practical application.

Using the catalytic system presented herein, neat furfural (1 mmol) (**18**) could be hydrogenated, but only moderate yields were achieved. Although benzaldehyde (**19**) could be reduced in high yield, vanillin (**20**) affords the corresponding alcohol in moderate yield, and both anisaldehyde (**21**) and syringaldehyde (**22**) gave very poor results. It seems that electron-donor groups deactivate the carbonyl moiety, preventing its hydrogenation.

The two catalytic materials studied herein differ in the nature of their stabilization, leading to distinct activities towards the hydrogenation of furfural (Fig. 9). RhNPs@SBA-15-Imz[NTf$_2$] achieved a TON of approximately 579, whereas RhNPs@SBA-15-NIC achieved a TON of only 289. The neutral and ionic nature of the silica grafting fragments showed a different role as stabilizers affecting the morphology and size of RhNPs, as shown in the Catalyst synthesis and characteriz-
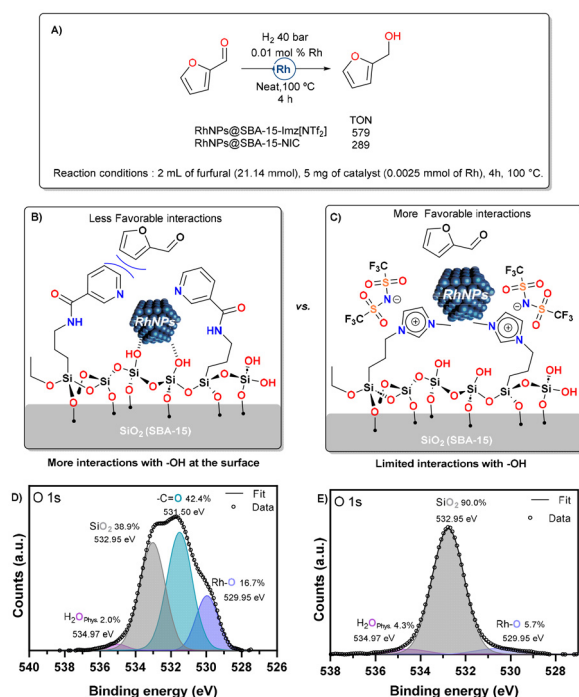
Fig. 9 (A) RhNP performance on furfural hydrogenation under neat conditions; proposed interactions of RhNPs with (B) SBA-15-NIC and (C) SBA-15-Imz[NTf$_2$] supports; high resolution XPS spectra of (D) RhNps@SBA-15-NIC and (E) RhNPs@SBA-15-Imz[NTf$_2$].

ation section. In addition, Supported Ionic Liquid Phases (SILPs) are able to modulate the chemical environment around active sites, controlling reaction selectivity in various cases.[89] In our study, the covalently supported imidazolium bistriflimide forms a thin IL layer, which upon RhNP formation, limits the interaction of Rh with silanol groups (Si–OH). High-resolution O 1s XPS spectra (Fig. 9E) reveal that only 6% of Rh–O species (529.95 eV)[90] are present, resulting in more favorable interactions with furfural and thus higher TONs. In contrast, the neutral nicotinamide fragment supported on silica does not form this thin layer, leading to greater metal–silanol interactions (17% Rh–O by XPS, Fig. 9D) that block the RhNP surface, thereby decreasing the TONs. This highlights the critical role of stabilizer choice in optimizing catalytic performance.

Conclusions

Overall, we synthesized RhNPs supported on N-functionalized silica-based materials. Specifically, we chose SBA-15 as the support and functionalized it with nicotinamide or an imidazolium-based ionic liquid. Solid-state ^{29}Si and ^{13}C NMR experiments confirmed the successful anchoring of the ligands to the silica surface. RhNPs@SBA-15-Imz[NTf$_2$] and RhNPs@SBA-15-NIC were easily prepared through organometallic precursor decomposition and thoroughly characterized. These materials exhibited small, spherical, and well-dis-

persed fcc Rh nanoparticles located on the support surface. XPS analyses revealed the presence of metallic rhodium, along with Rh(I) and Rh(III) species.

We then evaluated the catalytic performance of these materials in the hydrogenation of various functional groups, including alkenes, aldehydes, nitriles, ketones, nitro compounds, quinolines, and aromatic rings. Our particular focus was on the hydrogenation of biomass-derived substrates such as limonene, safrole, geraniol, levulinic acid, and furfural. Notably, the catalyst exhibited excellent recyclability, maintaining its activity and preventing metal leaching over multiple cycles.

In general, reactions involving excess amine poison the catalyst activity, preventing the reuse of the material.

Finally, the nature of the stabilization in RhNP catalysts significantly influences their activity towards furfural hydrogenation. RhNPs@SBA-15-Imz[NTf$_2$], with its ionic imidazolium bistriflimide stabilizer, limits silanol interactions with RhNPs, resulting in active systems for the hydrogenation of furfural. In contrast, RhNPs@SBA-15-NIC, with its neutral nicotinamide stabilizer, showed Rh–silanol interactions, blocking the RhNP surface and decreasing its catalytic activity. This highlights the critical role of stabilizer choice in optimizing catalytic performance.

Experimental section

General

Unless otherwise indicated, all manipulations and procedures were performed under a nitrogen atmosphere (99.998%) using standard Schlenk techniques. Organic solvents were distilled from appropriate desiccant under a nitrogen atmosphere and stored over activated 3 Å molecular sieves. All reagents were acquired from commercial suppliers and used as received. Microanalysis of the synthesized materials was carried out at USAII ("Unidad de Servicios de Apoyo a la Investigación y a la Industria" of the Faculty of Chemistry, UNAM). Infrared spectra were recorded on a PerkinElmer FTIR/FIR Spectrum 400 spectrometer. ^{1}H NMR, {^{1}H} COSY (Correlation Spectroscopy), ^{13}C{^{1}H} spectra were recorded on a JEOL ECZ600R spectrometer at 14.09 T (600 MHz for ^{1}H), and chemical shifts (δ, ppm) were calibrated relative to the residual solvent peak. Elemental analysis was carried out on a PerkinElmer 2400 Elemental Analyzer for CHNS using cysteine as the calibration compound. Thermogravimetric (TGA) data were recorded on a PerkinElmer TGA 4000 analyser from room temperature to 900 °C at a speed of 5 °C min^{-1}. For surface area analysis, a Micromeritics TriStar 3000 Surface Area and Pore Size Analyzer was used to produce nitrogen physisorption isotherms at 77 K on synthesized materials, and the data were fit using a Brunauer–Emmett–Teller (BET) model to determine the apparent surface areas of the materials. The average pore diameter and cumulative pore volumes were calculated using the Barrett–Joyner–Halenda (BJH) model for mesopores. Samples were degassed under vacuum at 130 °C for 18 h prior

to the analysis. Scanning electron microscopy (SEM) micrographs of synthesized materials were obtained on a JEOL JSM-5900-LV microscope. The particle diameter was determined by counting at least 100 individual particles with the software package Digimizer 4.6.1.[91] Transmission electron microscopy (TEM) images of the synthesized materials before and after recycling were obtained on a JEOL ARM200F microscope operating at an accelerating voltage of 200 kV. Nanoparticle measurements were performed with the software package DigitalMicrograph 3.30.2017.0.[92] XRD patterns were recorded on an X-ray powder diffractometer Bruker AXS model D8 advance Davinci (Theta-Theta configuration) equipped with a Lynxeye detector. The average MNP crystallite size was calculated from the full width at half maximum (FWHM) of the peaks using the Scherrer equation (eqn (1)).

$$\tau = \frac{K\lambda}{\beta \cos(\theta)} \tag{1}$$

where τ is the average crystallite size, K is a constant with a value of 0.9, λ is the X-ray wavelength, β is the FWHM in radians, and θ is the diffraction angle.

XPS measurements were performed using a Thermo Scientific K-Alpha spectrometer, with a MAGCIS ion source for depth profiling analysis and surface cleaning. The assignment of chemical components of core level Rh 3d was made by comparison to the referenced values reported in the literature.[53,93–95] Synthesis of supported rhodium nanoparticles was carried out in a 100 mL Fisher-Porter vessel. Catalytic reactions were performed in a Parr Multi Reactor 500 system. Catalytic conversions were determined on a Varian 3800 gas chromatograph with a capillary column DB-WAX (30 m × 0.32 mm × 0.25 mm) coupled to an FID detector, using the internal standard method.

Solid-state NMR spectra were recorded at the LCC (Toulouse) on a Bruker Avance 400 spectrometer equipped with 2.5, 3.2 or 4 mm probes. Samples were packed into 4 mm zirconia rotors. The rotors were spun at 8 kHz at 293 K. ^{13}C CP-MAS and ^{29}Si UDEFT-MAS spectra were recorded with a recycle delay of 2 s and contact times of 3 ms and 4 ms, respectively, and spectral deconvolution was fitted using the DMfit software.[96]

The precursor methoxy(1,5-cyclooctadiene)rhodium(ɪ) dimer [Rh(μ-OMe)(1,5-COD)]₂,[97] N-(3-(triethoxysilyl)propyl) nicotinamide, (NIC),[53,98] and 1-methyl-3-(3-(triethoxysilyl) propyl)-1H-imidazolium chloride[99] were prepared following the previously reported method.

SBA-15 was obtained according to Zhao *et al.*[100] The polymeric template was removed by calcination at 550 °C in air for 5 h, and the resulting synthesized rod-shaped mesoporous silica was denoted as SBA-15.

General synthesis of functionalized mesoporous silica SBA-15

In a Schlenk flask, SBA-15 (3 g) was dried at 80 °C for 24 h prior to use. Then, SBA-15 was suspended by sonication in dry toluene (140 mL) under nitrogen for 15 min, and then the mixture was treated with the corresponding silane (9.2 to 9.3 mmol, 100 wt% *vs.* SiO₂). The mixture was stirred at reflux temperature (120 °C) for 72 h. The solid was recovered by filtration and washed five times with hot toluene and ethanol. The resulting white solid dried under reduced pressure for 12 h.

SBA-15-Imz[NTf₂]

In addition to the above procedure, the material SBA-15-Imz [Cl] was further treated with LiNTf₂ for salt metathesis. Briefly, under nitrogen, the solid obtained SBA-15-Imz[Cl] was resuspended in dry dichloromethane and treated with an excess of bis(trifluoromethane)sulfonimide lithium salt (1.5 g, 5.2 mmol). The mixture was stirred at room temperature (*ca.* 25 °C) for 72 h. The solid was separated by filtration and washed five times with hot dry ethanol. The obtained solid was dried under reduced pressure for 12 h.

FT-IR(ATR) ν (cm^{-1}): 3300 (ν SiO–H), 2900–2800 (ν C–H), 1574 (ν C=N imz), 1345 (ν S=O), 1184 (ν C–F), 1034 (ν Si–O–Si), 444 (ν Si–O). TGA: 32.9 wt% organic content. **Elem. anal. found** C, 11.71; H, 2.08; N, 3.75; S, 2.63. ^{13}C {^{1}H} CP-MAS (100 MHz, ppm): 135.71 (N–CH–N, Imz), 122.16 (N–CH–CH–N, Imz), 117.80 (–CF₃, NTf₂), 58.16 (SiO–CH₂–CH₃), 50.80 (N–CH₂–), 35.12 (–N–CH₃), 22.91 (Si–CH₂–CH₂–CH₂–N), 14.85 (SiO–CH₂–CH₃), 8.27 (–CH₂–Si–). ^{29}Si UDEFT-MAS (79 MHz, ppm) δ: −58.80 (T^2), −68.57 (T^3), −92.41 (Q^2), −101.68 (Q^3), −109.58 (Q^4).

SBA-15-NIC

FT-IR(ATR) ν (cm^{-1}): 3300 (ν SiO–H), 2900–2800 (ν C–H), 1646 (ν C=O), 1545 (δ N–H), 1060 (ν Si–O–Si), 705 (γ N–H), 440 (ν Si–O). **TGA:** 25.11 wt% organic content. **Elem. anal. found** C, 13.44; H, 2.25; N, 4.35. ^{13}C {^{1}H} CP-MAS (100 MHz, ppm): 163.44 (–C=O), 147.78 (–CH–, Py), 144.05 (–CH–, Py), 136.6 (–CH–, Py), 128.41 (C *ipso*, Py), 124.20 (–CH–, Py), 57.52 (SiO–CH₂–CH₃), 41.87 (–HN–CH₂–), 20.93 (CH₂–CH₂–CH₂), 16.09 (SiO–CH₂–CH₃), 9.45 (–CH₂–Si–). ^{29}Si UDEFT-MAS (79 MHz, ppm) δ: −59.10 (T^2), −67.54 (T^3), −92.59 (Q^2), −101.68 (Q^3), −109.61 (Q^4).

General synthesis of supported RhNPs on functionalized silicas

In a Fisher-Porter reactor, [Rh(μ-OMe)(1,5-COD)]₂ (105.9 mg, 0.219 mmol) and 405 mg of functionalized silica (SBA-15-NIC or SBA-15-Imz[NTf₂]) were suspended in dry THF (50 mL) under a nitrogen atmosphere. This mixture was sonicated for five minutes to obtain a homogeneous pale-yellow suspension. The reactor was then charged with 3 bar of H₂ at room temperature and allowed to stir for 18 h. After the reaction time, the reactor was depressurized, and all volatiles were removed under reduced pressure to afford a black solid. The supported RhNPs (black solid) obtained were dried under vacuum at 80 °C for 24 h.

General procedure for catalytic hydrogenation reactions

5 mg of RhNPs@SBA-15-Imz[NTf$_2$] or RhNPs@SBA-15-NIC was added to a 25 mL stainless steel reactor flask equipped with glass liner and a stirring magnet, together with a solvent (2 mL) and substrate(s) (2 mmol). The reaction mixture was then pressurized with hydrogen (5, 20 or 40 bar) and stirred (300 rpm) at 100 °C for the specified time. After the reaction was completed, the reactor vessel was cooled with an ice bath and slowly depressurized. The crude product was filtered through a Celite® pad prior to being analysed by GC. For acidic substrates, *i.e.* levulinic acid or oleic acid, a 100 mL Hastelloy® reactor with glass liner was employed.

Data availability

The data supporting this article have been included as part of the ESI.†

Conflicts of interest

The authors declare no competing financial interest.

References

1 A. J. Ragauskas, C. K. Williams, B. H. Davison, G. Britovsek, J. Cairney, C. A. Eckert, W. J. Frederick, J. P. Hallett, D. J. Leak, C. L. Liotta, J. R. Mielenz, R. Murphy, R. Templer and T. Tschaplinski, The Path Forward for Biofuels and Biomaterials, *Science*, 2006, **311**, 484–489, DOI: **10.1126/science.1114736**.

2 G. W. Huber, S. Iborra and A. Corma, Synthesis of Transportation Fuels from Biomass: Chemistry, Catalysts, and Engineering, *Chem. Rev.*, 2006, **106**, 4044–4098, DOI: **10.1021/cr068360d**.

3 A. Corma, S. Iborra and A. Velty, Chemical Routes for the Transformation of Biomass into Chemicals, *Chem. Rev.*, 2007, **107**, 2411–2502, DOI: **10.1021/cr050989d**.

4 J. C. Colmenares, R. S. Varma and V. Nair, Selective photo-catalysis of lignin-inspired chemicals by integrating hybrid nanocatalysis in microfluidic reactors, *Chem. Soc. Rev.*, 2017, **46**, 6675–6686, DOI: **10.1039/C7CS00257B**.

5 C. Li, X. Zhao, A. Wang, G. W. Huber and T. Zhang, Catalytic Transformation of Lignin for the Production of Chemicals and Fuels, *Chem. Rev.*, 2015, **115**, 11559–11624, DOI: **10.1021/acs.chemrev.5b00155**.

6 Y. Jing, L. Dong, Y. Guo, X. Liu and Y. Wang, Chemicals from Lignin: A Review of Catalytic Conversion Involving Hydrogen, *ChemSusChem*, 2020, **13**, 4181–4198, DOI: **10.1002/cssc.201903174**.

7 C. P. Xu, R. A. D. Arancon, J. Labidi and R. Luque, Lignin depolymerisation strategies: towards valuable chemicals and fuels, *Chem. Soc. Rev.*, 2014, **43**, 7485–7500, DOI: **10.1039/C4CS00235K**.

8 L. Shuai, M. T. Amiri, Y. M. Questell-Santiago, F. Héroguel, Y. Li, H. Kim, R. Meilan, C. Chapple, J. Ralph and J. S. Luterbacher, Formaldehyde stabilization facilitates lignin monomer production during biomass depolymerization, *Science*, 2016, **354**, 329–333, DOI: **10.1126/science.aaf7810**.

9 X. Wu, X. Fan, S. Xie, J. Lin, J. Cheng, Q. Zhang, L. Chen and Y. Wang, Solar energy-driven lignin-first approach to full utilization of lignocellulosic biomass under mild conditions, *Nat. Catal.*, 2018, **1**, 772–780, DOI: **10.1038/s41929-018-0148-8**.

10 Y. Nakagawa and K. Tomishige, Production of 1,5-penta-nediol from biomass via furfural and tetrahydrofurfuryl alcohol, *Catal. Today*, 2012, **195**(1), 136–143, DOI: **10.1016/j.cattod.2012.04.048**.

11 B. Abdullah, S. A. F. A. S. Muhammad and N. A. N. Mahmood, Production of Biofuel via Hydrogenation of Lignin from Biomass in *New Advances, in Hydrogenation Processes: Fundamental and Applications*, ed. M. T. Ravanchi, IntechOpen, 2017, pp. 289–305. DOI: **10.5772/66108**.

12 X. Jin, T. Fang, J. Wang, M. Liu, S. Pan, B. Subramaniam, J. Shen, C. Yang and R. V. Chaudhari, Nanostructured Metal Catalysts for Selective Hydrogenation and Oxidation of Cellulosic Biomass to Chemicals, *Chem. Rec.*, 2019, **19**(9), 1952–1994, DOI: **10.1002/tcr.201800144**.

13 K. Tomishige, N. Nakagawa and M. Tamura, Selective hydrogenolysis and hydrogenation using metal catalysts directly modified with metal oxide species, *Green Chem.*, 2017, **19**, 2876–2924, DOI: **10.1039/C7GC00620A**.

14 A. Racha, C. Samanta, S. Sreekantan and B. Marimuthu, Review on Catalytic Hydrogenation of Biomass-Derived Furfural to Furfuryl Alcohol: Recent Advances and Future Trends, *Energy Fuels*, 2023, **37**(16), 11475–11496, DOI: **10.1021/acs.energyfuels.3c01174**.

15 M. Schlaf, Selective deoxygenation of sugar polyols to a,w-diols and other oxygen content reduced materials—a new challenge to homogeneous ionic hydrogenation and hydrogenolysis catalysis, *Dalton Trans.*, 2006, 4645–4653, DOI: **10.1039/B608007C**.

16 A. Bordet, G. Moos, C. Welsh, P. Licence, K. L. Luska and W. Leitner, Molecular Control of the Catalytic Properties of RhodiumNanoparticles in Supported Ionic Liquid Phase (SILP) Systems, *ACS Catal.*, 2020, **10**, 13904–13912, DOI: **10.1021/acscatal.0c03559**.

17 Y. Zhang, A. Li, M. Kubu, M. Shamzhy and J. Cejka, Highly selective reduction of biomass-derived furfural by tailoring the microenvironment of Rh@BEA catalysts, *Catal. Today*, 2022, **390–391**, 295–305, DOI: **10.1016/j.cattod.2021.09.031**.

18 S. Liu, N. Govindarajan and K. Chan, Understanding Activity Trends in Furfural Hydrogenation on Transition Metal Surfaces, *ACS Catal.*, 2022, **12**(20), 12902–12910, DOI: **10.1021/acscatal.2c03822**.

19 J. Lee, Y. Xu and G. W. Huber, High-throughput screening of monometallic catalysts for aqueous-phase hydrogenation of biomass-derived oxygenates, *Appl. Catal., B*, 2013, **140–141**, 98–107, DOI: **10.1016/j.apcatb.2013.03.031**.

20 M. Balakrishanan, E. R. Sacia and A. T. Bell, Selective Hydrogenation of Furan-Containing Condensation Products as a Source of Biomass-Derived Diesel Additives, *ChemSusChem*, 2014, **7**(10), 2796–2800, DOI: **10.1002/cssc.201402764**.

21 Y. Luo, J. Yi, D. Tong and C. Hu, Production of γ-valerolactone via selective catalytic conversion of hemicellulose in pubescens without addition of external hydrogen, *Green Chem.*, 2016, **18**, 848–857, DOI: **10.1039/C5GC01775K**.

22 M. Li, G. Li, N. Li, A. Wang, W. Dong, X. Wang and Y. Cong, Aqueous phase hydrogenation of levulinic acid to 1,4-pentanediol, *Chem. Commun.*, 2014, **50**, 1414–1416, DOI: **10.1039/C3CC48236G**.

23 C. Ban, W. Jeon, H. C. Woo and D. H. Kim, Catalytic Hydrogenation of Macroalgae-Derived Alginic Acid into Sugar Alcohols, *ChemSusChem*, 2017, **10**(24), 4891–4898, DOI: **10.1002/cssc.201701860**.

24 Y. Duan, C. Zhang, D. Deng, D. Sui, X. Gao and Y. Yang, Hydrogenation of BHMF with controllable selectivity to tetrahydropyranone and 1-hydroxy-2,5-hexanedione under atmospheric H2 pressure, *Green Chem.*, 2023, **25**, 1823–1834, DOI: **10.1039/D2GC04637G**.

25 L. L. R. Vono, C. Broicher, K. Philippot and L. M. Rossi, Tuning the selectivity of phenol hydrogenation using Pd, Rh and Ru nanoparticles supported on ceria- and titania-modified silicas, *Catal. Today*, 2021, **381**, 126–132, DOI: **10.1016/j.cattod.2020.07.078**.

26 Y. Song, O. Y. Gutiérrez, J. Herranz and J. A. Lercher, Aqueous phase electrocatalysis and thermal catalysis for the hydrogenation of phenol at mild conditions, *Appl. Catal., B*, 2016, **182**, 236–246, DOI: **10.1016/j.apcatb.2015.09.027**.

27 C. Yu, W. Wu, M. Gao and Y. Liu, Modified Cellulose with BINAP-Supported Rh as an Efficient Heterogeneous Catalyst for Asymmetric Hydrogenation, *Catalysts*, 2022, **12**, 83, DOI: **10.3390/catal12010083**.

28 A. Vandekerkhove, L. Claes, F. De Shouwer, C. Van Goethem, I. F. J. Vankelecom, B. Lagrain and D. E. De Vos, Rh-Catalyzed Hydrogenation of Amino Acids to Biobased Amino Alcohols: Tackling Challenging Substrates and Application to Protein Hydrolysates, *ACS Sustainable Chem. Eng.*, 2018, **6**(7), 9218–9228, DOI: **10.1021/acssuschemeng.8b01546**.

29 I. Toth, J. M. Tukacs and L. T. Mika, Kinetic and Mechanistic Studies of the Selective Hydrogenation of (E)-Chalcones in Biomass-Derived γ-Valerolactone Catalyzed by Rh–PPh3 Complexes, *ChemCatChem*, 2023, **15**(7), e202201480, DOI: **10.1002/cctc.202201480**.

30 G. Zou, W. Zhong, L. Mao, Q. Xu, J. Xiao, D. Yin, Z. Xiao, S. R. Kirk and T. Shu, A non-nitric acid method of adipic acid synthesis: organic solvent- and promoter-free oxidation of cyclohexanone with oxygen over hollow-structured Mn/TS-1 catalysts, *Green Chem.*, 2015, **17**, 1884–1892, DOI: **10.1039/C4GC02333A**.

31 P. Etayo and A. Vidal-Ferran, Rhodium-catalysed asymmetric hydrogenation as a valuable synthetic tool for the preparation of chiral drugs, *Chem. Soc. Rev.*, 2013, **42**, 728–754, DOI: **10.1039/C2CS35410A**.

32 S. K. Murphy, J.-W. Park, F. A. Cruz and V. M. Dong, Rh-catalyzed C–C bond cleavage by transfer hydroformylation, *Science*, 2015, **347**, 56–60, DOI: **10.1126/science.1261232**.

33 *Rhodium Catalysed hydroformylation*, ed. P. W. N. M. Van Leeuwen and C. Claver, Kluwer Academic Publishers, New York, 2002.

34 A. Pérez-Alonso, D. P. Minh, D. Pla and M. Gómez, A Cooperative Rh/Co-Catalyzed Hydroaminomethylation Reaction for the Synthesis of Terpene Amines, *ChemCatChem*, 2023, **15**(13), e202300501, DOI: **10.1002/cctc.202300501**.

35 J. Dupont and J. D. Scholtten, On the structural and surface properties of transition-metal nanoparticles in ionic liquids, *Chem. Soc. Rev.*, 2010, **39**, 1780–1804, DOI: **10.1039/B822551F**.

36 A. Serrano-Maldonado, A. Reina, B. Portales-Martínez and I. Guerrero-Ríos, Thioglycerol-Stabilized Rhodium Nanoparticles in Biphasic Medium as Catalysts in Multistep Reactions, *Eur. J. Inorg. Chem.*, 2020, **26**, 2506–2511, DOI: **10.1002/ejic.202000451**.

37 A. Serrano-Maldonado, T. Dang-Bao, I. Favier, I. Guerrero-Ríos, D. Pla and M. Gómez, Glycerol Boosted Rh-

Catalyzed Hydroaminomethylation Reaction: A Mechanistic Insight, *Chem. – Eur. J.*, 2020, **26**, 12553–12559, DOI: **10.1002/chem.202001978**.

38 M. J. Ndolomingo, B. Ndzondelelo and R. Meijboom, Review of supported metal nanoparticles: synthesis methodologies, advantages and application as catalysts, *J. Mater. Sci.*, 2020, **55**, 6195–6241, DOI: **10.1007/s10853-020-04415-x**.

39 S. Ganji, S. S. Enumula, R. K. Marella, K. S. R. Rao and D. R. Burri, RhNPs/SBA-NH2: a high-performance catalyst for aqueous phase reduction of nitroarenes to aminoarenes at room temperature, *Catal. Sci. Technol.*, 2014, **4**, 1813–1819, DOI: **10.1039/C4CY00143E**.

40 E. Vunain, P. Ncube, K. Jalama and R. Meijboom, Confinement effect of rhodium(I) complex species on mesoporous MCM-41 and SBA-15: effect of pore size on the hydroformylation of 1-octene, *J. Porous Mater.*, 2018, **25**, 303–320, DOI: **10.1007/s10934-017-0443-9**.

41 I. Choi, S. Chun and Y. K. Chung, Bimetallic Cobalt–Rhodium Nanoparticle-Catalyzed Reductive Amination of Aldehydes with Nitroarenes Under Atmospheric Hydrogen, *J. Org. Chem.*, 2017, **82**, 12771–12777, DOI: **10.1021/acs.joc.7b02019**.

42 L. Huang, Z. Wang, L. Geng, R. Chen, W. Xing, Y. Wang and J. Huang, Selective and recyclable rhodium nanocatalysts for the reductive N-alkylation of nitrobenzenes and amines with aldehydes, *RSC Adv.*, 2015, **5**, 56936–56941, DOI: **10.1039/C5RA05243B**.

43 M. Muñoz, Z. M. de Pedro, J. A. Casas and J. J. Rodríguez, Improved γ-alumina-supported Pd and Rh catalysts for hydrodechlorination of chlorophenols, *Appl. Catal., A*, 2014, **488**, 78–85, DOI: **10.1016/j.apcata.2014.09.035**.

44 S. Sharma, D. Bhattacherjee and P. Das, Supported Rhodium Nanoparticles Catalyzed Reduction of Nitroarenes, Arylcarbonyls and Aryl/Benzyl Sulfoxides using Ethanol/Methanol as In Situ Hydrogen Source, *Adv. Synth. Catal.*, 2018, **360**(11), 2131–2137, DOI: **10.1002/adsc.201701609**.

45 N. Pal and A. Bhaumik, Mesoporous materials: versatile supports in heterogeneous catalysis for liquid phase catalytic transformations, *RSC Adv.*, 2015, **5**, 24363–24391, DOI: **10.1039/C4RA13077D**.

46 R. J. Witzke, A. Chapovetsky, M. P. Conley, D. M. Kaphan and M. Delferro, Nontraditional Catalyst Supports in Surface Organometallic Chemistry, *ACS Catal.*, 2020, **10**(20), 11822–11840, DOI: **10.1021/acscatal.0c03350**.

47 J. Liang, Z. Liang, R. Zou and Y. Zhao, Heterogeneous Catalysis in Zeolites, Mesoporous Silica, and Metal–Organic Frameworks, *Adv. Mater.*, 2017, **29**, 1701139, DOI: **10.1002/adma.201701139**.

48 S. Chongdar, S. Bhattacharjee, P. Bhanja and A. Bhaumik, Porous organic–inorganic hybrid materials for catalysis, energy and environmental applications, *Chem. Commun.*, 2022, **58**, 3429–3460, DOI: **10.1039/D1CC06340E**.

49 J. Sharma and G. Plizos, Hollow Silica Particles: Recent Progress and Future Perspectives, *Nanomaterials*, 2020, **10**(8), 1599, DOI: **10.3390/nano10081599**.

50 C. Coperet, A. Comas-Vives, M. P. Conley, D. P. Estes, A. Fedorov, V. Mougel, H. Nagae, F. Nunez-Zarur and P. A. Zhizhko, Surface Organometallic and Coordination Chemistry toward Single-Site Heterogeneous Catalysts: Strategies, Methods, Structures, and Activities, *Chem. Rev.*, 2016, **116**(2), 323–421, DOI: **10.1021/acs.chemrev.5b00373**.

51 B. C. Gates, M. Flytzani-Stephanopoulos, D. A. Dixon and A. Katz, Atomically dispersed supported metal catalysts: perspectives and suggestions for future research, *Catal. Sci. Technol.*, 2017, **7**(19), 4259–4275, DOI: **10.1039/C7CY00881C**.

52 A. Reina, R. Carmona-Chávez, I. T. Pulido-Díaz, D. Martínez, K. P. Salas-Martin and I. Guerrero-Ríos, Silica-Supported 1st Row Transition Metal (Nano) Catalysts: Synthetic and Catalytic Insight, *ChemCatChem*, 2023, **15**(11), e202300285, DOI: **10.1002/cctc.202300285**.

53 I. T. Pulido-Díaz, A. Serrano-Maldonado, C. C. López-Suárez, P. A. Méndez-Ocampo, B. Portales-Martínez, A. Gutiérrez-Alejandre, K. P. Salas-Martin and I. Guerrero-Ríos, RhNPs supported on N-functionalized mesoporous silica: effect on catalyst stabilization and catalytic activity, *Dalton Trans.*, 2021, **50**, 3289–3298, DOI: **10.1039/D0DT04213G**.

54 K. L. Luska, A. Bordet, S. Tricard, I. Sinev, W. Grünert, B. Chaudret and W. Leitner, Enhancing the Catalytic Properties of Ruthenium Nanoparticles-SILP Catalysts by Dilution with Iron, *ACS Catal.*, 2016, **6**(6), 3719–3726, DOI: **10.1021/acscatal.6b00796**.

55 S. Rengshausen, C. Van Stappen, N. Levin, S. Tricard, K. L. Luska, S. DeBeer, B. Chaudret, A. Bordet and W. Leitner, Organometallic Synthesis of Bimetallic Cobalt-Rhodium Nanoparticles in Supported Ionic Liquid Phases $(Co_xRh_{100-x}@SILP)$ as Catalysts for the Selective Hydrogenation of Multifunctional Aromatic Substrates, *Small*, 2021, **17**(5), 2006683, DOI: **10.1002/smll.202006683**.

56 V. H. Paschoal, L. F. O. Faria and M. C. C. Ribeiro, Vibratonal Spectroscopy of Ionic Liquids, *Chem. Rev.*, 2017, **117**(10), 7053–7112, DOI: **10.1021/acs.chemrev.6b00461**.

57 I. S. Protsak, Y. M. Morozov, W. Dong, Z. Le, D. Zhang and I. M. Henderson, A ^{29}Si, ^1H, and ^{13}C Solid-State NMR Study on the Surface Species of Various Depolymerized Organosiloxanes at Silica Surface, *Nanoscale Res. Lett.*, 2019, **14**, 160, DOI: **10.1186/s11671-019-2982-2**.

58 N. T. Duong, J. Trébosc, O. Lafon and J.-P. Amoureux, Improved Sensitivity and Quantification for 29Si NMR Experiments on Solids Using UDEFT (Uniform Driven Equilibrium Fourier Transform), *Solid State Nucl. Magn. Reson.*, 2019, **100**, 52–62, DOI: **10.1016/j.ssnmr.2019.03.007**.

59 X. Wang, S. Cheng and J. C. C. Chan, Propylsulfonic Acid-Functionalized Mesoporous Silica Synthesized by in Situ Oxidation of Thiol Groups under Template-Free Condition, *J. Phys. Chem. C*, 2007, **111**(5), 2156–2164, DOI: **10.1021/jp066924b**.

60 M. J. Cleare and W. P. Griffith, Infrared spectra of isotopically substituted nitro-, nitrito-, and nitrosyl complexes,

J. Chem. Soc. A, 1967, 1144–1147, DOI: 10.1039/J19670001144.

61 P. Schneider, Adsorption isotherms of microporous-mesoporous solids revisited, *Appl. Catal., A*, 1995, **129**(2), 157–165, DOI: 10.1016/0926-860X(95)00110-7.

62 M. Thommes, K. Kaneko, A. V. Neimark, J. P. Oliver, F. Rodríguez-Reinoso, J. Rouquerol and K. S. W. Sing, Physisorption of gases, with special reference to the evaluation of surface area and pore size distribution (IUPAC Technical Report), *Pure Appl. Chem.*, 2015, **87**, 1051–1069, DOI: 10.1515/pac-2014-1117.

63 L. Zhu, S. Ye, J. Zhu, C. Duan, K. Li, G. He and X. Liu, Tartaric Acid-Assisted Synthesis of Well-Dispersed Ni Nanoparticles Supported on Hydroxyapatite for Efficient Phenol Hydrogenation, *ACS Sustainable Chem. Eng.*, 2022, **10**, 10526–10536, DOI: 10.1021/acssuschemeng.2c01642.

64 T. C. Nugent and M. El-Shazly, Chiral Amine Synthesis – Recent Developments and Trends for Enamide Reduction, Reductive Amination, and Imine Reduction, *Adv. Synth. Catal.*, 2010, **352**(5), 753–819, DOI: 10.1002/adsc.200900719.

65 M. Haniti, A. Hamid, C. L. Allen, G. W. Lamb, A. C. Maxwell, H. C. Maytum, A. J. A. Watson and J. M. J. Williams, Ruthenium-Catalyzed N-Alkylation of Amines and Sulfonamides Using Borrowing Hydrogen Methodology, *J. Am. Chem. Soc.*, 2009, **131**, 1766–1774, DOI: 10.1021/ja807323a.

66 V. R. Jumde, E. Petricci, C. Petrucci, N. Santillo, M. Taddei and L. Vaccaro, Domino Hydrogenation–Reductive Amination of Phenols, a Simple Process To Access Substituted Cyclohexylamines, *Org. Lett.*, 2015, **17**, 3990–3993, DOI: 10.1021/acs.orglett.5b01842.

67 B. Zheng, J. Song, H. Wu, S. Han, J. Zhai, K. Zhang, W. Wu, C. Xu, M. He and B. Han, Palladium-catalyzed synthesis of 4-cyclohexylmorpholines from reductive coupling of aryl ethers and lignin model compounds with morpholines, *Green Chem.*, 2021, **23**, 268–273, DOI: 10.1039/D0GC03188G.

68 B. Zheng, H. Wu, J. Song, W. Wu, X. Mei, K. Zhang, C. Xu, J. Xu, M. He and B. Han, Production of alkoxyl-functionalized cyclohexylamines from lignin-derived guaiacols, *Green Chem.*, 2021, **23**, 8441–8447, DOI: 10.1039/D1GC02790E.

69 Z. Chen, H. Zeng, H. Gong, H. Wang and C.-J. Li, Palladium-catalyzed reductive coupling of phenols with anilines and amines: efficient conversion of phenolic lignin model monomers and analogues to cyclohexylamines, *Chem. Sci.*, 2015, **6**, 4174–4178, DOI: 10.1039/C5SC00941C.

70 V. Bragonia, R. K. Rit, R. Kirchmann, A. S. Trita and L. J. Goossen, Synthesis of bio-based surfactants from cashew nutshell liquid in water, *Green Chem.*, 2018, **20**, 3210–3213, DOI: 10.1039/C8GC01686K.

71 T. L. Lohr, Z. Li, R. S. Assary, L. A. Curtiss and T. J. Marks, Thermodynamically Leveraged Tandem Catalysis for Ester RC(O)O–R′ Bond Hydrogenolysis, Scope and Mechanism,

ACS Catal., 2015, **5**(6), 3675–3679, DOI: 10.1021/acscatal.5b00950.

72 L. Yan, X.-X. Liu and Y. Fu, N-Alkylation of amines with phenols over highly active heterogeneous palladium hydride catalysts, *RSC Adv.*, 2016, **6**, 109702–109705, DOI: 10.1039/C6RA22383D.

73 T. Cuypers, T. Morias, S. Windels, C. Marquez, C. Van Goethem, I. Vankelecom and D. E. De Vos, Ni-Catalyzed reductive amination of phenols with ammonia or amines into cyclohexylamines, *Green Chem.*, 2020, **22**, 1884–1893, DOI: 10.1039/C9GC02625H.

74 M. Ortega, R. Manrique, R. Jiménez, M. Parreño, M. E. Domine and L. E. Arteaga-Pérez, Secondary Amines from Catalytic Amination of Bio-Derived Phenolics over Pd/C and Rh/C: Effect of Operation Parameters, *Catalysts*, 2023, **13**(4), 654, DOI: 10.3390/catal13040654.

75 C. Chaudhari, K. Sato, S. Rumi, Y. Nishida, M. Shiraishi and K. Nagaoka, Rh-PVP Catalyzed Reductive Amination of Phenols by Ammonia or Amines to Cyclohexylamines under Solvent-free Conditions, *Chem. Lett.*, 2022, **51**(1), 81–84, DOI: 10.1246/cl.210574.

76 V. Mévellec, A. Nowicki, A. Roucoux, C. Dujardin, P. Granger, E. Payen and K. Philippot, A simple and reproducible method for the synthesis of silica-supported rhodium nanoparticles and their investigation in the hydrogenation of aromatic compounds, *New J. Chem.*, 2006, **30**, 1214–1219, DOI: 10.1039/B605893K.

77 J. Llop Castelbou, E. Bresó-Femenia, P. Blondeau, B. Chaudret, S. Castillón, C. Claver and C. Godard, Tuning the Selectivity in the Hydrogenation of Aromatic Ketones Catalyzed by Similar Ruthenium and Rhodium Nanoparticles, *ChemCatChem*, 2014, **6**(11), 3160–3168, DOI: 10.1002/cctc.201402524.

78 D. B. Bagal and B. M. Bhanage, Recent Advances in Transition Metal-Catalyzed Hydrogenation of Nitriles, *Adv. Synth. Catal.*, 2015, **357**, 883–900, DOI: 10.1002/adsc.201400940.

79 D. Formenti, R. Mocci, H. Atia, S. Dastgir, M. Anwar, S. Bachmann, M. Scalone, K. Junge and M. Beller, A State-of-the-Art Heterogeneous Catalyst for Efficient and General Nitrile Hydrogenation, *Chem. – Eur. J.*, 2020, **26**, 15589–15595, DOI: 10.1002/chem.202001866.

80 F. Liu, M. Audemar, K. De Oliveira Vigier, J.-M. Clacenc, F. De Campo and F. Jérome, Combination of Pd/C and Amberlyst-15 in a single reactor for the acid/hydrogenating catalytic conversion of carbohydrates to 5-hydroxy-2,5-hexanedione, *Green Chem.*, 2014, **16**, 4110–4114, DOI: 10.1039/C4GC01158A.

81 Y. Nakagawa, M. Tamura and K. Tomishige, Catalytic Reduction of Biomass-Derived Furanic Compounds with Hydrogen, *ACS Catal.*, 2013, **3**, 2655–2668, DOI: 10.1021/cs400616p.

82 M. Hronec, K. Fulajtarova and T. Liptaj, Effect of catalyst and solvent on the furan ring rearrangement to cyclopentanone, *Appl. Catal., A*, 2012, **437–438**, 104–111, DOI: 10.1016/j.apcata.2012.06.018.

83 P. Reyes, D. Salinas, C. Campos, M. Oportus, J. Murcia, H. Rojas, G. Borda and J. L. G. Fierro, Selective hydrogenation of furfural on Ir/TiO2 catalysts, *Quim. Nova*, 2010, **33**, 777–780, DOI: **10.1590/S0100-40422010000400002**.

84 W. Yu, Y. Tang, L. Mo, P. Chen, H. Lou and X. Zheng, One-step hydrogenation–esterification of furfural and acetic acid over bifunctional Pd catalysts for bio-oil upgrading, *Bioresour. Technol.*, 2011, **102**, 8241–8246, DOI: **10.1016/j.biortech.2011.06.015**.

85 V. V. Ordomsky, J. C. Schouten, J. Van der Schaaf and T. A. Nijhuis, Biphasic single-reactor process for dehydration of xylose and hydrogenation of produced furfural, *Appl. Catal., A*, 2013, **451**, 6–13, DOI: **10.1016/j.apcata.2012.11.013**.

86 S. P. Lee and Y. W. Chen, Selective Hydrogenation of Furfural on Ni–P, Ni–B, and Ni–P–B Ultrafine Materials, *Ind. Eng. Chem. Res.*, 1999, **38**, 2548–2556, DOI: **10.1021/ie990071a**.

87 M. Audemar, C. Ciotonea, K. De Oliveira Vigier, S. Royer, A. Ungureanu, B. Dragoi, E. Dumitriu and F. Jérome, Selective Hydrogenation of Furfural to Furfuryl Alcohol in the Presence of a Recyclable Cobalt/SBA-15 Catalyst, *ChemSusChem*, 2015, **8**, 1885–1891, DOI: **10.1002/cssc.201403398**.

88 C. K. P. Neeli, Y.-M. Chung and W.-S. Ahn, Catalytic Transfer Hydrogenation of Furfural to Furfuryl Alcohol by using Ultrasmall Rh Nanoparticles Embedded on Diamine-Functionalized KIT-6, *ChemCatChem*, 2017, **9**, 4570–4579, DOI: **10.1002/cctc.201701037**.

89 P. Migowski, P. Lozano and J. Dupont, Imidazolium based ionic liquid-phase green catalytic reactions, *Green Chem.*, 2023, **25**(4), 1237–1260, DOI: **10.1039/D2GC04749G**.

90 C. Sleigh, A. P. Pijpers, A. Jaspers, B. Coussens and R. J. Meier, On the Determination of Atomic Charge via ESCA Including Application to Organometallics, *J. Electron Spectrosc. Relat. Phenom.*, 1996, **77**(1), 41–57, DOI: **10.1016/0368-2048(95)02392-5**.

91 *Digimizer 4.6.1*, MedCalc Software, Belgium, 2005–2012.

92 *DigitalMicrograph 3.30.2017.0*, Gatan Inc., 1996–2018.

93 A. M. Dennis, R. A. Howard, K. M. Kadish, J. L. Bear, J. Brace and N. Winograd, X-Ray Photoelectron Spectra of Some Dirhodium Carboxylate Complexes, *Inorg. Chim. Acta*, 1980, **44**, 139–141, DOI: **10.1016/S0020-1693(00)90981-2**.

94 M. Carvalho, L. F. Wieserman and D. M. Hercules, Spectroscopic Characterization of Wilkinson's Catalyst Using X-ray Photoelectron Spectroscopy (ESCA), *Appl. Spectrosc.*, 1982, **36**, 290–296.

95 Y. Abe, K. Kato, M. Kawamura and K. Sasaki, Rhodium and Rhodium Oxide Thin Films Characterized by XPS, *Surf. Sci. Spectra*, 2001, **8**, 117–125, DOI: **10.1116/11.20010801**.

96 D. Massiot, F. Fayon, M. Capron, I. King, S. Le Calvé, B. Alonso, J.-O. Durand, B. Bujoli, Z. Gan and G. Hoatson, Modelling one- and two-dimensional solid-state NMR spectra, *Magn. Reson. Chem.*, 2002, **40**, 70–76, DOI: **10.1002/mrc.984**.

97 R. Uson, L. A. Oro, J. A. Cabeza, H. E. Bryndza and M. P. Stepro, Dinuclear Methoxy, Cyclooctadiene, and Barrelene Complexes of Rhodium(I) and Iridium(I), *Inorg. Synth.*, 1985, **23**, 126–130, DOI: **10.1002/9780470132548.ch25**.

98 G. Singh, S. Rani, A. Saroa, Promila, A. Arora and D. Choquesillo-Lazarte, Amide-tethered organosilatranes: Syntheses, structural characterization and photophysical properties, *Inorg. Chim. Acta*, 2015, **433**, 78–91, DOI: **10.1016/j.ica.2015.04.034**.

99 J. Brünig, Z. Csendes, S. Weber, N. Gorgas, R. W. Bittner, A. Limbeck, K. Bica, H. Hoffmann and K. Kirchner, Chemoselective Supported Ionic-Liquid-Phase (SILP) Aldehyde Hydrogenation Catalyzed by an Fe(II) PNP Pincer Complex, *ACS Catal.*, 2018, **8**(2), 1048–1051, DOI: **10.1021/acscatal.7b04149**.

100 D. Zhao, Q. Huo, J. Feng, B. F. Chmelka and G. D. Stucky, Nonionic Triblock and Star Diblock Copolymer and Oligomeric Surfactant Syntheses of Highly Ordered, Hydrothermally Stable, Mesoporous Silica Structures, *J. Am. Chem. Soc.*, 1998, **120**(24), 6024–6036, DOI: **10.1021/ja974025i**.